Article

Rapid Microwave-Assisted Synthesis of $ZnIn_2S_4$ Nanosheets for Highly Efficient Photocatalytic Hydrogen Production

Yu-Cheng Chang [1,*] **, Yung-Chang Chiao** [1] **and Po-Chun Hsu** [2]

1. Department of Materials Science and Engineering, Feng Chia University, Taichung 407102, Taiwan; d0455077@gmail.com
2. Pritzker School of Molecular Engineering, University of Chicago, Chicago, IL 60637, USA; pochunhsu@uchicago.edu
* Correspondence: yuchchang@fcu.edu.tw

Abstract: In this study, a facile and rapid microwave-assisted synthesis method was used to synthesize In_2S_3 nanosheets, ZnS nanosheets, and $ZnIn_2S_4$ nanosheets with sulfur vacancies. The two-dimensional semiconductor photocatalysts of $ZnIn_2S_4$ nanosheets were characterized by XRD, FESEM, BET, TEM, XPS, UV–vis diffuse reflectance, and PL spectroscopy. The $ZnIn_2S_4$ with sulfur vacancies exhibited an evident energy bandgap value of 2.82 eV, as determined by UV–visible diffuse reflectance spectroscopy, and its energy band diagram was obtained through the combination of XPS and energy bandgap values. $ZnIn_2S_4$ nanosheets exhibited about 33.3 and 16.6 times higher photocatalytic hydrogen production than In_2S_3 nanosheets and ZnS nanosheets, respectively, under visible-light irradiation. Various factors, including materials, sacrificial reagents, and pH values, were used to evaluate the influence of $ZnIn_2S_4$ nanosheets on photocatalytic hydrogen production. In addition, the $ZnIn_2S_4$ nanosheets revealed the highest photocatalytic hydrogen production from seawater, which was about 209.4 and 106.7 times higher than that of In_2S_3 nanosheets and ZnS nanosheets, respectively. The presence of sulfur vacancies in $ZnIn_2S_4$ nanosheets offers promising opportunities for developing highly efficient and stable photocatalysts for photocatalytic hydrogen production from seawater under visible-light irradiation.

Keywords: $ZnIn_2S_4$ nanosheets; microwave-assisted synthesis; sacrificial reagents; photocatalytic hydrogen production; seawater

1. Introduction

Microwave-assisted synthesis is a popular technique for the rapid and facile preparation of organic/inorganic nanostructured materials in various media [1,2]. In addition, it offers control for internal and volumetric heating of materials, making it an environmentally friendly method for fabricating new material structures, components, and devices [3]. Microwave-assisted synthesis has been widely used to synthesize nanostructured materials, including metals, nanoporous materials, colloidal nanocrystals, polymer nanocomposites, and inorganic or semiconducting nanomaterials [2,4–9]. Microwave-assisted synthesis of nanostructures offers several advantages, including contactless heat transfer to the reactant sample, short reaction time, high selectivity and yield, energy efficiency, uniform and selective distribution of energy, control over size and temperature, improved safety and reproducibility, and excellent control over experimental parameters, making it an inexpensive, quick, clean, and versatile technique for the preparation of nanostructures [10–14]. In addition, microwave-assisted synthesis has distinct characteristics that render it viable for achieving extensive-scale industrial manufacturing [15,16].

Zinc indium sulfide ($ZnIn_2S_4$) is a highly efficient two-dimensional semiconductor photocatalyst from the AB_2X_4 family of ternary compounds, widely used in solar energy conversion and environmental purification [17–20]. $ZnIn_2S_4$ typically forms two-dimensional nanosheets due to its layered crystal structure, but these nanosheets quickly

aggregate and assemble into three-dimensional nanostructures to minimize the surface energy for most reported $ZnIn_2S_4$ [19,21]. $ZnIn_2S_4$ has two crystal structures: hexagonal and cubic, with hexagonal $ZnIn_2S_4$ being the most researched in photocatalysis [22–24]. Recently, $ZnIn_2S_4$ has gained attention in photocatalytic hydrogen production, carbon dioxide conversion, and pollutant removal, owing to its excellent light absorption and strong redox capabilities [25–28]. However, the low separation degree of photogenerated charge carriers and the low electron-transport efficiency of $ZnIn_2S_4$ limit its application in photocatalysis [29]. In order to improve photocatalytic efficiency, introducing sulfur or zinc vacancies has proven effective [30,31]. So far, most of the research on $ZnIn_2S_4$ has focused on combining different materials to improve its photocatalytic hydrogen production performance, but there are few reports on preparing $ZnIn_2S_4$ with sulfur defects via the microwave-assisted synthesis method [32].

Previous research has reported significant instances of photocatalytic hydrogen production, predominantly employing deionized or pure water [33,34]. Nevertheless, the preparation of deionized or pure water necessitates the purification of fresh water, which results in energy wastage and contributes to the depletion of freshwater resources [35,36]. Furthermore, the increasing occurrence of abnormal climate changes, such as heavy rainfall or drought, has led to a scarcity of freshwater resources [37,38]. Consequently, developing a photocatalyst capable of effectively decomposing seawater to generate hydrogen would address this challenge and further enhance the situation [39]. Therefore, this study aimed to produce hydrogen through the photocatalytic decomposition of seawater using $ZnIn_2S_4$ nanosheets with sulfur defects, potentially reducing freshwater consumption and addressing the scarcity of freshwater resources.

This study successfully synthesized In_2S_3 nanosheets, ZnS nanosheets, and $ZnIn_2S_4$ nanosheets with sulfur vacancies for photocatalytic hydrogen production by microwave-assisted synthesis. The photocatalytic activities of $ZnIn_2S_4$ nanosheets with sulfur vacancies were approximately 33.3 times higher than those of In_2S_3 nanosheets and about 16.6 times higher than those of ZnS nanosheets under visible-light irradiation. Notably, utilizing $ZnIn_2S_4$ nanosheets with sulfur vacancies as a photocatalyst demonstrated their exceptional performance in efficiently splitting seawater under visible-light irradiation.

2. Materials and Methods

2.1. Chemicals

Anhydrous zinc chloride ($ZnCl_2$, 98%), anhydrous indium(III) chloride ($InCl_3$, 98%), thioacetamide (TAA, C_2H_5NS, 98%), sodium sulfide nonahydrate ($Na_2S·9H_2O$, 98%), sodium sulfite (Na_2SO_3, 98%), methanoic acid (CH_2O_2, 97%), folic acid dihydrate ($C_{19}H_{19}N_7O_6·2H_2O$, 97%), methanol (CH_3OH, 99%), and sodium chloride (NaCl, 99%) were purchased from Alfa Aesar (Haverhill, MA, USA) without further purification. Deionized water (>18 MΩ·cm) was used throughout the experimental processes.

2.2. Synthesis of In_2S_3, $ZnIn_2S_4$, and ZnS Nanosheets

A facile microwave-assisted synthesis method can be used to synthesize In_2S_3 nanosheets, $ZnIn_2S_4$ nanosheets, and ZnS nanosheets. For In_2S_3 nanosheets, 0.0045 g of $InCl_3$ and 0.0075 g of TAA were dissolved in the 20 mL solvent (deionized water: ethanol = 3:1) and put into a Teflon-lined digestion vessel. For $ZnIn_2S_4$ nanosheets, 0.0068 g of $ZnCl_2$, 0.0045 g of $InCl_3$, and 0.0075 gTAA were dissolved in the 20 mL solvent (deionized water: ethanol = 3:1) and put into the Teflon-lined digestion vessel. For ZnS nanosheets, 0.0136 g of $ZnCl_2$, and 0.0075 g TAA were dissolved in the 20 mL solvent (deionized water: ethanol = 3:1) and put into the Teflon-lined digestion vessel. A safety shield was placed around the vessel after sealing the reaction solution inside the vessel, using the vessel cover as an overpressure release valve. The vessel was then heated at 140 °C for 1 h using a microwave synthesizer (ETHOS EASY, Milestone, Sorisole, Italy). Following the cooling stage, the as-prepared samples were thoroughly cleaned with deionized water, purified through centrifugation, and dried at 70 °C for 2 h.

2.3. Characterization

The crystal structure of the as-prepared photocatalysts was investigated by X-ray diffractometry (XRD) using a Bruker D2 phaser system (Billerica, MA, USA) in the 2θ range of 25–65° with Cu Kα (λ = 1.5418 Å). In addition, field-emission scanning electron microscopy (FESEM) was used to investigate the surface morphology of the as-prepared photocatalysts using a Hitachi S-4800 microscope (Tokyo, Japan) operating at a 15 kV accelerating voltage. The specific surface areas of the as-prepared photocatalysts were measured using the nitrogen adsorption technique (ASAP 2020, Micromeritics, GA, USA). Field-emission transmission electron microscopy (FETEM) at an accelerating voltage of 200 kV was employed to characterize the microstructures and composition of the $ZnIn_2S_4$ nanosheets using a JEOL 2100F microscope (Tokyo, Japan). The surface chemical composition and sulfur vacancies of the $ZnIn_2S_4$ nanosheets were detected by using X-ray photoelectron spectroscopy (XPS, ULVAC-PHI PHI 5000 Versaprobe II system, Chigasaki, Japan) with an Al K source. The as-prepared photocatalysts' UV–vis diffuse reflectance spectra were recorded using a UV–vis spectrophotometer (PerkinElmer Lambda 650 S, Waltham, MA, USA) and analyzed using a Protrustech MRI532S instrument (Tainan, Taiwan). A three-electrode system was utilized with the assistance of the Zennium electrochemical workstation (Zahhner, Kronach, Germany) for measuring electrochemical impedance spectroscopy (EIS).

*2.4. Photocatalytic Hydrogen Production Experiment*

In order to investigate photocatalytic hydrogen production, an experiment was conducted with the PCX50B Discover photocatalytic reaction system (Perfect Light Technology, Beijing, China). For the experiment, 25 mg of the as-prepared photocatalysts was mixed with 50 mL of different water bases, including deionized water, reverse-osmosis water, tap water, and seawater. Different sacrificial agents, such as sodium sulfide, sodium sulfate, methanol, and methanoic acid, were added to the water bases at 0.1 M concentrations. The mixtures were then placed in 60 mL quartz tubes, and Ar gas was introduced for 30 min to eliminate air. The tubes were sealed with rubber stoppers and irradiated for 3 h using a 5 W blue LED (λ = 420 nm) as a visible-light source. The hydrogen produced was quantified using a gas chromatograph equipped with a thermal conductivity detector (TCD).

3. Results and Discussion

The crystalline phases of the prepared photocatalysts were analyzed using X-ray diffraction (XRD). Figure 1 shows the XRD patterns of In_2S_3 nanosheets, $ZnIn_2S_4$ nanosheets, and ZnS nanosheets grown via rapid microwave-assisted synthesis at 140 °C for 1 h. For In_2S_3 nanosheets (Figure 1a), the eight peaks at 27.7°, 28.9°, 33.6°, 43.9°, 48.0°, 51.9°, 56.3°, and 59.8° correspond to the (311), (222), (400), (511), (440), (610), (533), and (444) planes of typical cubic In_2S_3 (JCPDS card No. 32-0456), respectively. For $ZnIn_2S_4$ nanosheets (Figure 1b), the five peaks at 27.7°, 28.8°, 47.3°, 52.2°, and 56.4°correspond to the (102), (103), (110), (1012), and (203) planes of typical hexagonal $ZnIn_2S_4$ (JCPDS card No. 72-0773), respectively. For ZnS nanosheets (Figure 1c), the four peaks at 27.7°, 28.8°, 47.3°, and 56.4°correspond to the (100), (002), (110), and (112) planes of typical hexagonal ZnS (JCPDS card No. 80-0007), respectively. The absence of diffraction peaks corresponding to impurities further confirms the phase purity of the prepared photocatalysts.

The surface morphologies of the synthesized In_2S_3 nanosheets, $ZnIn_2S_4$ nanosheets, and ZnS nanosheets were characterized using FESEM, as depicted in Figure 2. In Figure 2a, small and interconnected In_2S_3 nanosheets can be observed, and the thickness of the nanosheets is about 15–40 nm. $ZnIn_2S_4$ nanosheets are larger and interconnected, with a thickness of about 15–60 nm, as shown in Figure 2b. Figure 2c reveals that the ZnS nanosheets are stacked on one another and form a spherical structure. We utilized a BET (Brunauer–Emmett–Teller) analyzer to examine the specific surface areas of In_2S_3 nanosheets, $ZnIn_2S_4$ nanosheets, and ZnS nanosheets. The nitrogen adsorption–desorption isotherms revealed that the specific surface areas of these photocatalysts were as follows:

99.8 (In_2S_3 nanosheets), 77.3 ($ZnIn_2S_4$ nanosheets), and 35.8 (ZnS nanosheets) m^2g^{-1}. The specific surface areas of the In_2S_3 nanosheets and $ZnIn_2S_4$ nanosheets were significantly larger than that of the ZnS nanosheets, which is consistent with the FESEM characterization results.
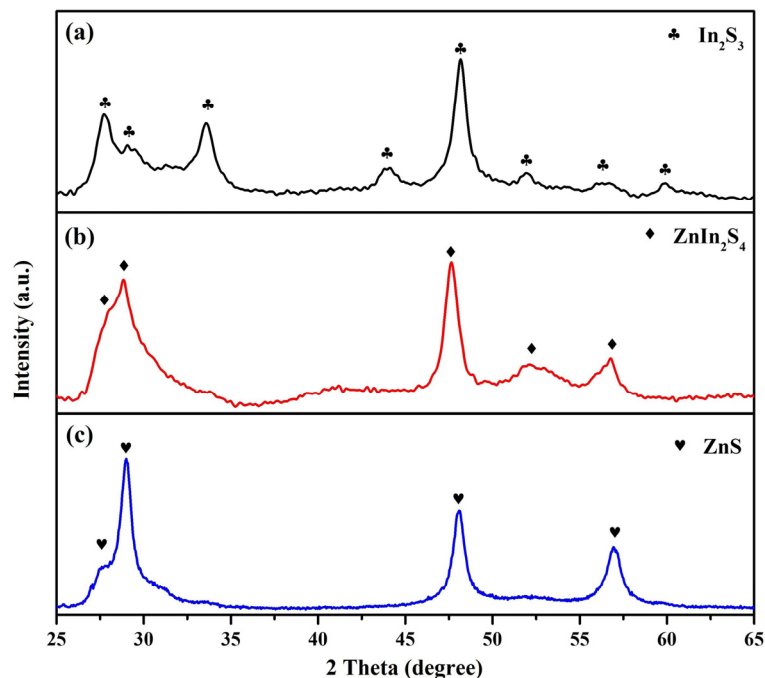
**Figure 1.** The XRD patterns of (**a**) In_2S_3 nanosheets, (**b**) $ZnIn_2S_4$ nanosheets, and (**c**) ZnS nanosheets.
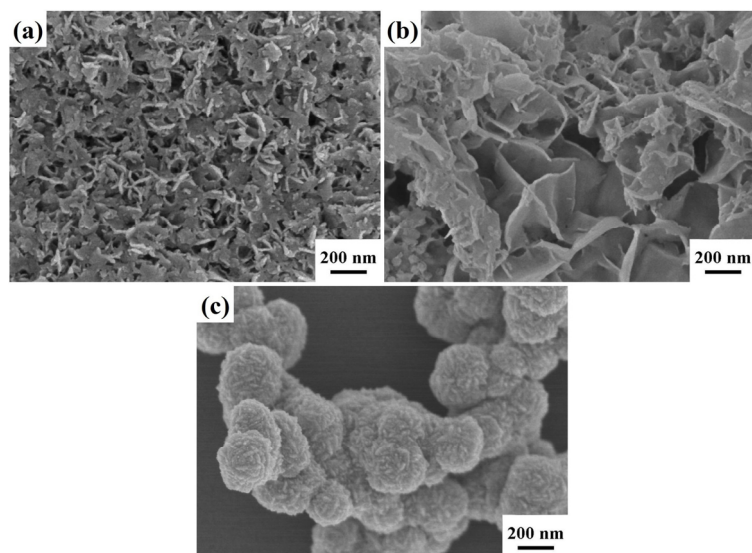
Figure 2. The FESEM images of (**a**) In_2S_3 nanosheets, (**b**) $ZnIn_2S_4$ nanosheets, and (**c**) ZnS nanosheets.

Figure 3a shows the FETEM image of $ZnIn_2S_4$ nanosheets, which is consistent with the FESEM image of the nanosheet structure made of lamellar stacks. Additionally, the polycrystalline nature of the $ZnIn_2S_4$ nanosheets is substantiated by the presence of characteristic polycrystalline diffraction rings observed in the selected-area electron diffraction (SAED) patterns, as shown in Figure 3b. The prominent diffraction ring patterns correspond to the crystal planes (102), (103), (110), (1012), and (203), which are indicative of the typical hexagonal structure of $ZnIn_2S_4$ (JCPDS card No. 72-0773). These findings are consistent with the results obtained from the XRD analysis, confirming the polycrystalline properties of the $ZnIn_2S_4$ nanosheets. Figure 3c reveals that the HRTEM image of the lattice

fringes of 0.331 nm and 0.322 nm are assigned to the (101) and (102) planes of hexagonal $ZnIn_2S_4$, respectively. Moreover, the mapping images obtained from the energy-dispersive spectrometry (EDS) analysis (Figure 3d) reveal a uniform and interconnected distribution of elemental Zn, In, and S. These results provide conclusive evidence of the successful synthesis of $ZnIn_2S_4$ nanosheets.
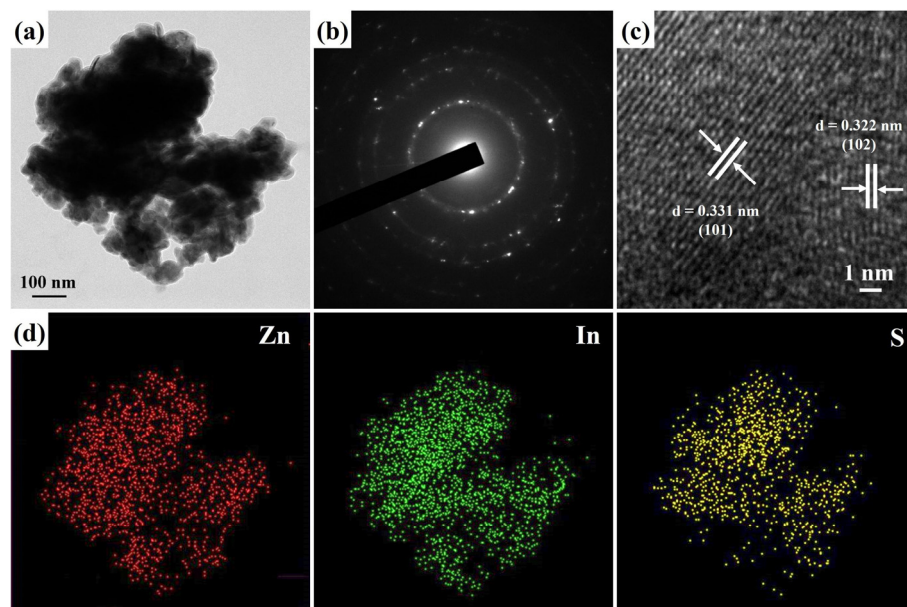
Figure 3. (**a**) FETEM, (**b**) SAED, (**c**) HRTEM, and (**d**) EDS mapping images of $ZnIn_2S_4$ nanosheets.

X-ray photoelectron spectroscopy (XPS) was utilized to determine the elemental composition and chemical configurations of the $ZnIn_2S_4$ nanosheets. Figure 4a displays the complete XPS spectrum, which confirms the presence of elemental Zn, In, S, C, and O in the $ZnIn_2S_4$ nanosheets. The appearance of C 1s and O 1s signals can be explained by the presence of pump oil in the XPS equipment's vacuum system and the adsorption of oxygen atoms, respectively. Figure 4b shows that the high-resolution XPS spectrum of Zn 2p reveals two peaks at 1021.2 eV and 1044.2 eV, which are assigned to Zn $2p_{3/2}$ and Zn $2p_{1/2}$, respectively, indicating the presence of Zn^{2+} in $ZnIn_2S_4$. Figure 4c shows that the high-resolution XPS spectrum of In 3d reveals two peaks at 444.2 eV and 451.8 eV, which are assigned to In $3d_{5/2}$ and In $3d_{3/2}$, respectively, indicating the presence of In^{3+} in $ZnIn_2S_4$. Compared with pure $ZnIn_2S_4$ (S $2p_{1/2}$ = 161.4 eV and S $2p_{3/2}$ = 162.7 eV), the XPS peaks of S $2p_{1/2}$ and $2p_{3/2}$ in $ZnIn_2S_4$ nanosheets with sulfur defects shift to lower binding energies of 160.9 and 161.9 eV, respectively [25,31,40]. This peak shift can primarily be attributed to the presence of sulfur vacancies, indicating the influence of these vacancies on the electronic structure of the materials [41]. This result demonstrates that rapid microwave-assisted synthesis can facilitate the formation of $ZnIn_2S_4$ nanosheets with sulfur defects during the same reaction process.

In order to assess the photocatalytic characteristics of the catalyst, a photocatalytic hydrogen evolution experiment was conducted in deionized water. The hydrogen evolution rate (HER) activities of the as-prepared photocatalysts (In_2S_3 nanosheets, $ZnIn_2S_4$ nanosheets, and ZnS nanosheets) and commercial photocatalysts (ZnO nanopowder and TiO_2 nanopowder) were evaluated under visible-light irradiation (5 W blue LED, λ = 420 nm) using 0.1 M Na_2S as a sacrificial reagent in deionized water with pH = 12, as shown in Figure 5a. The $ZnIn_2S_4$ nanosheets exhibited an HER value of 24.95 $\mu molh^{-1}g^{-1}$, which is about 33.3 and 16.6 times higher than 0.75 (In_2S_3 nanosheets) and 1.5 (ZnS nanosheets) $\mu molh^{-1}g^{-1}$, respectively. On the other hand, the pure $ZnIn_2S_4$ nanosheets synthesized by a hydrothermal method revealed significantly lower HER values of 0.065 $\mu molh^{-1}g^{-1}$ under the same photocatalytic reaction conditions [25]. These outcomes indicate that uti-

lizing the rapid microwave-assisted synthesis approach facilitates the growth of $ZnIn_2S_4$ nanosheets with sulfur vacancies, leading to a notable improvement in their photocatalytic hydrogen evolution.
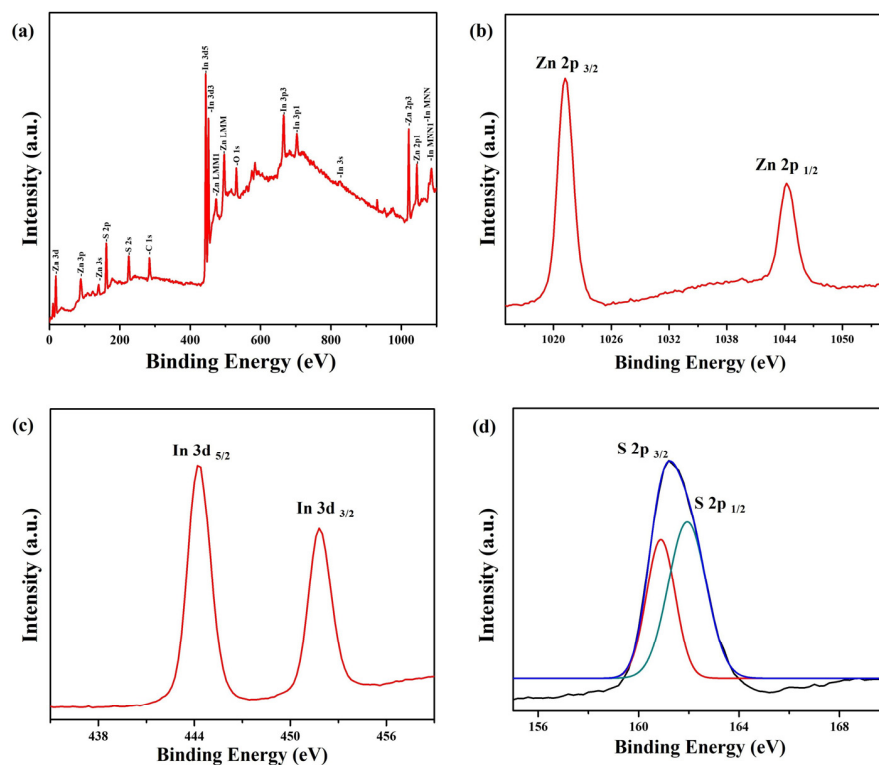

Figure 4. XPS spectra of the $ZnIn_2S_4$ nanosheets: (**a**) survey spectrum, (**b**) Zn 2p, (**c**) In 3d, and (**d**) S 2p.
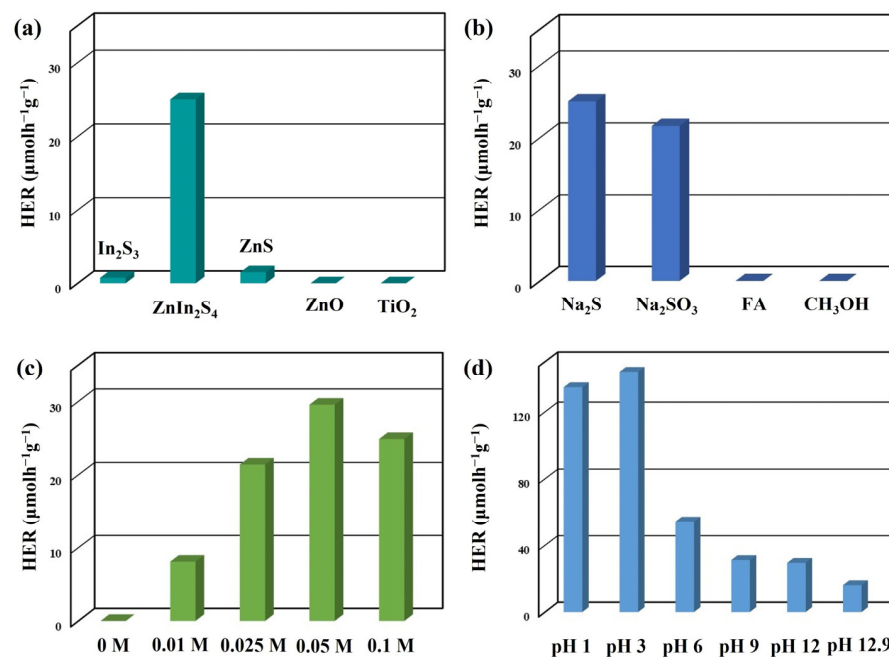

Figure 5. (**a**) The average HER of different photocatalysts. The average HER of $ZnIn_2S_4$ nanosheets under the different photocatalytic reaction conditions: (**b**) sacrificial reagents, (**c**) Na_2S concentrations, and (**d**) pH values.

In photocatalytic hydrogen production, sacrificial reagents are often employed to enhance the efficiency of oxidation reactions in aqueous environments, compensating

for the inefficiency of pure water oxidation [42]. Figure 5b illustrates the HER values of $ZnIn_2S_4$ nanosheets under visible-light irradiation using four different sacrificial reagents: sodium sulfide (Na_2S), sodium sulfite (Na_2SO_3), folic acid (FA), and methanol (CH_3OH). The HER values of the $ZnIn_2S_4$ nanosheets were 24.95 (Na_2S), 21.6 (Na_2SO_3), 0 (FA), and 0 $\mu molh^{-1}g^{-1}$ (CH_3OH). In photocatalytic hydrogen generation, the sacrificial agent serves the dual role of providing electrons for proton reduction and scavenging holes to impede the recombination of electron–hole pairs, thereby improving the process's efficiency [43,44]. Consequently, using sodium sulfide or sodium sulfate as a sacrificial reagent can enhance the reduction/oxidation reaction, reduce the photocorrosion of metal sulfide materials, and enhance their photocatalytic hydrogen production capability [42,45].

In general, concentrated sacrificial reagents are preferable, as they promote better diffusion of the reacting species toward the surface of the photocatalysts [46,47]. However, it is essential to note that the highest hydrogen evolution rate cannot be achieved with diluted or highly concentrated sacrificial reagents [48]. The impact of Na_2S concentrations on the photocatalytic efficiency of $ZnIn_2S_4$ nanosheets is shown in Figure 5c. The average HER values of the $ZnIn_2S_4$ nanosheets were recorded as follows: 0 (without Na_2S), 8.1 (0.01 M Na_2S), 21.4 (0.025 M Na_2S), 29.55 (0.05 M Na_2S), and 24.95 $\mu molh^{-1}g^{-1}$ (0.1 M Na_2S). The $ZnIn_2S_4$ nanosheets with appropriate Na_2S concentrations can exhibit the highest HER under visible-light irradiation.

The optimal pH level for photocatalytic hydrogen production is primarily determined by the characteristics of the sacrificial agent and its affinity for adsorption onto the surface of the photocatalyst [49]. The impact of pH values on the photocatalytic efficiency of $ZnIn_2S_4$ nanosheets is illustrated in Figure 5d. The average HER values of $ZnIn_2S_4$ nanosheets were recorded as follows: 134.5 (pH = 1), 143.9 (pH = 3), 54.4 (pH = 6), 31.25 (pH = 9), 29.55 (pH = 12), and 16.3 $\mu molh^{-1}g^{-1}$ (pH = 12.9, without adjustment). An increase in the pH value from 1 to 3 significantly enhanced the photocatalytic hydrogen production efficiency. This enhancement can be attributed to the increased dissociation of HS^- and S^{2-} species with the increasing pH value [47]. However, low pH values may result in photocorrosion of the catalyst and a reduction in hydrogen production efficiency [35]. Hence, the $ZnIn_2S_4$ nanosheets exhibited the highest photocatalytic hydrogen production efficiency at pH = 3.

The UV–vis diffuse reflectance spectra of In_2S_3, $ZnIn_2S_4$, and ZnS nanosheets within the range of 300–800 nm are illustrated in Figure 6a. For In_2S_3 nanosheets, a pronounced absorption can be observed below 600 nm, indicating strong intrinsic interband transition absorption specific to In_2S_3. For $ZnIn_2S_4$ nanosheets, a notable absorption can be observed below 500 nm, corresponding to the intrinsic interband transition absorption of In_2S_3. Finally, for ZnS nanosheets, a significant absorption can be observed below 400 nm in the UV region, attributed to the intrinsic interband transition absorption of ZnS. These observations indicate that both In_2S_3 nanosheets and $ZnIn_2S_4$ nanosheets exhibit substantial absorption of visible light. The direct optical bandgap, E_g, of the materials was determined by employing the equation $(\alpha h\nu)^2 = A(h\nu - E_g)$, where $h\nu$ represents the photon energy in electron volts (eV), α is the absorption coefficient, and A is a material constant [50]. This analysis was conducted based on the data presented in Figure 6b. Consistent with prior findings, the results indicate that the In_2S_3, $ZnIn_2S_4$, and ZnS bandgaps were measured to be 2.05 eV, 2.82 eV, and 3.32 eV, respectively [25,51,52].

Photoluminescence (PL) spectra are a valuable tool for examining photogenerated charge carriers' trapping, migration, and transfer efficiency in semiconductors [53,54]. By analyzing the PL spectra, it is possible to gain insights into the recombination and annihilation processes of photogenerated electron–hole pairs in semiconductors [55]. Figure 7a displays the PL spectra of In_2S_3, $ZnIn_2S_4$, and ZnS nanosheets. The ZnS nanosheets demonstrate more pronounced emission characteristics than the In_2S_3 and $ZnIn_2S_4$ nanosheets, suggesting a higher degree of recombination of photogenerated charge carriers within the photocatalyst. Electrochemical impedance spectroscopy (EIS) is presented in Figure 7b. The arc radii of the EIS Nyquist curves of the samples were in the following order: ZnS > In_2S_3 > $ZnIn_2S_4$. $ZnIn_2S_4$'s arc radius was smaller than those of In_2S_3 and ZnS.

The smaller radius observed in the EIS test indicates lower charge transfer resistance and higher efficiency in separating charge carriers, suggesting a faster electron transfer process [56–58]. Consequently, the EIS results confirm that $ZnIn_2S_4$ nanosheets with sulfur vacancies facilitate the migration of photogenerated charge carriers, resulting in enhanced photocatalytic activity for hydrogen evolution.
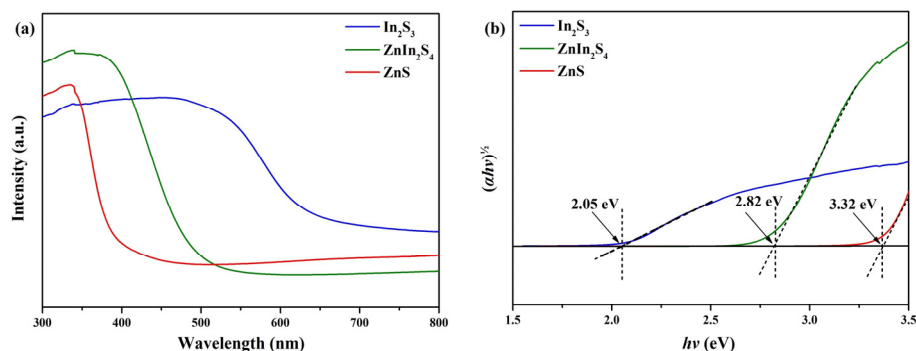
Figure 6. (**a**) UV–vis diffuse reflectance spectra and (**b**) Tauc plot of In_2S_3, $ZnIn_2S_4$, and ZnS nanosheets.
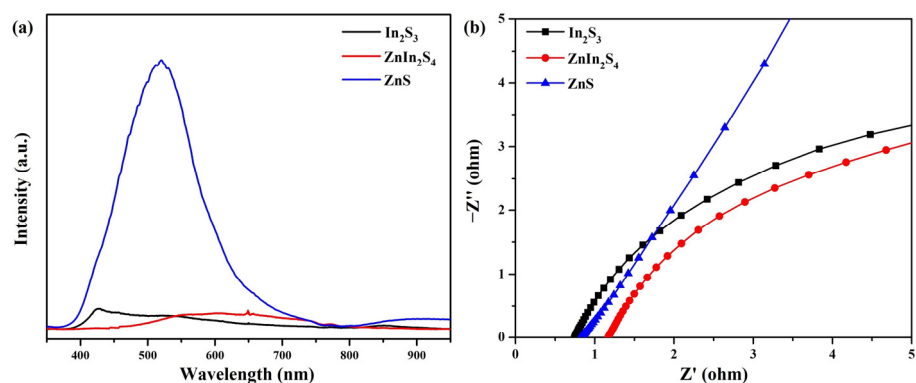

Figure 7. (**a**) PL and (**b**) EIS spectra of In_2S_3, $ZnIn_2S_4$, and ZnS nanosheets.

The band structure greatly influences the generation and migration of charge carriers. Therefore, the valence band (VB) XPS was conducted on the obtained $ZnIn_2S_4$ nanosheets to investigate the valence band location. Figure 8a illustrates the typical valence band density of states (DOS) characteristics of $ZnIn_2S_4$ nanosheets with the valence band position at 0.76 eV. Based on the equation $E_{CB} = E_{VB} - E_g$ and the measured bandgap of $ZnIn_2S_4$ (Figure 6b), the conduction band (CB) potential is estimated to occur at -2.06 eV. After carefully examining the findings above, we developed a hypothetical reaction mechanism for photocatalytic hydrogen production using $ZnIn_2S_4$ nanosheets. The proposed mechanism is visually depicted in Figure 8b, providing a realistic representation of the process. The presence of sulfur vacancies in $ZnIn_2S_4$ leads to the formation of defect levels within the conduction band (CB). In addition, these sulfur vacancies act as electron traps, effectively capturing photogenerated electrons and preventing their direct recombination with photoinduced holes. The trapped electrons in the sulfur vacancies of $ZnIn_2S_4$ can subsequently participate in the reduction of $2H^+$ to produce H_2. At the same time, the photogenerated holes in $ZnIn_2S_4$ can oxidize sulfide ions (S^{2-}, sodium sulfide dissociated).

Given that approximately 93% of the Earth's water exists in the form of seawater, utilizing seawater as a source for hydrogen production through water splitting offers a practical solution to conserve freshwater resources for various purposes, such as agriculture, industry, and human consumption [39,59]. Furthermore, the hydrogen produced through the photocatalytic decomposition of seawater can be utilized to generate pure water through a fuel cell generator, adding to its potential benefits. The exceptional versatility of $ZnIn_2S_4$ nanosheets is demonstrated by their photocatalytic capability to generate hydrogen using

various water sources. As depicted in Figure 9a, the dispersion of $ZnIn_2S_4$ nanosheets in 50 mL of different water sources, including deionized water (DI), reverse-osmosis water (RO), tap water (TW), and seawater (SW), was observed under visible-light irradiation with a pH value of 3 and the presence of 0.1 M Na_2S as a scavenger. The average HER values of $ZnIn_2S_4$ nanosheets were measured as 143.9 (DI), 158.9 (RO), 207.7 (TW), and 992.4 $\mu molh^{-1}g^{-1}$ (SW). With the increasing complexity of the water matrix, there is a gradual enhancement in the efficiency of photocatalytic hydrogen production. In order to investigate the influence of sodium chloride (NaCl) on the photocatalytic effect, this study included the addition of 35 psu NaCl (35 g/L) to deionized water to assess its impact on hydrogen production, as shown in Figure 9b. This result indicates that adding sodium chloride to deionized water did not significantly improve the efficiency of photocatalytic hydrogen production. Therefore, it can be inferred that sodium chloride might not be the primary factor for enhancing photocatalytic hydrogen production. The average HER values of photocatalysts, such as In_2S_3 nanosheets, $ZnIn_2S_4$ nanosheets, ZnS nanosheets, ZnO nanopowder, and TiO_2 nanopowder, were assessed under visible-light irradiation using 0.1 M Na_2S as a sacrificial reagent in seawater with a pH value of 3, as depicted in Figure 9c. The average HER values of the photocatalysts were measured as 4.74 (In_2S_3 nanosheets), 992.4 ($ZnIn_2S_4$ nanosheets), 9.3 (ZnS nanosheets), 3.7 (ZnO nanopowder), and 0 $\mu molh^{-1}g^{-1}$ (TiO_2 nanopowder). The $ZnIn_2S_4$ nanosheets exhibited the highest photocatalytic hydrogen production from seawater, which was about 209.4 and 106.7 times higher than that of In_2S_3 nanosheets and ZnS nanosheets, respectively. These results demonstrate that the microwave-assisted synthesis method promotes the formation of $ZnIn_2S_4$ nanosheets with sulfur vacancies, significantly enhancing their photocatalytic activity for hydrogen production from seawater.
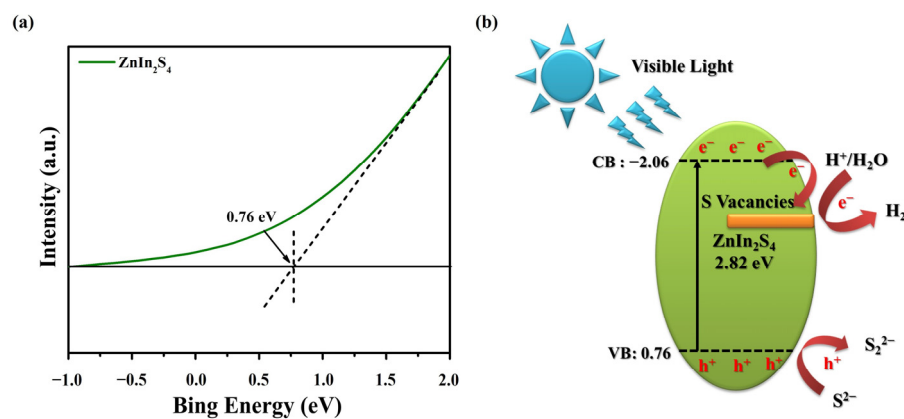

Figure 8. (**a**) VB XPS spectrum of the $ZnIn_2S_4$ nanosheets. (**b**) The schematic diagram depicts the charge separation process and photocatalytic reaction in the $ZnIn_2S_4$ nanosheets under visible-light irradiation.

The reusability of $ZnIn_2S_4$ nanosheets was investigated through an eight-cycle photocatalytic process, wherein the seawater containing 0.1 M Na_2S at pH = 3 was renewed and subjected to visible-light irradiation, as shown in Figure 10. As a result, the average HER values of $ZnIn_2S_4$ nanosheets were recorded as follows: 992.4, 1277.5, 1445.6, 1694.8, 1782.3, 1688.2, 1676.9, and 1518.0 $\mu molh^{-1}g^{-1}$. The photocatalytic hydrogen production efficiency from seawater exhibited an initial increase followed by a gradual decline as the number of cycles increased. The HER of $ZnIn_2S_4$ nanosheets showed a notable increase of 1.8 times after the fifth cycle compared to the first cycle. A noticeable distinction was observed between the XRD spectrum before the cycle (Figure 1b) and after the eighth cycle (Figure 11a). Notably, three additional crystal phases of ZnS (JCPDS card No. 72-0163), Zn_2SO_4 (JCPDS card No. 86-0802), and $NaZn(OH)_3$ (JCPDS card No. 87-0762) were identified following the cycling process. This phenomenon can be attributed to the interaction between $ZnIn_2S_4$ nanosheets and seawater, forming $ZnIn_2S_4/ZnS$ nanocomposites. ZnS

possesses sulfur vacancies at the defect level, which can facilitate the migration of photo-generated charge carriers to enhance photocatalytic performance [60,61]. The morphology of $ZnIn_2S_4$ nanosheets exhibited similarity before the cycle (Figure 2b) and after the eighth cycle (Figure 11b), and noticeable changes were obtained in the roughness of the surface following the cycling process. However, a slight decrease in HER was observed in the sixth cycle, possibly due to the loss of photocatalysts during multiple centrifugations. Furthermore, these results confirm the outstanding stability and reusability of $ZnIn_2S_4$ nanosheets, highlighting their potential for wide-ranging and diverse applications in various fields.
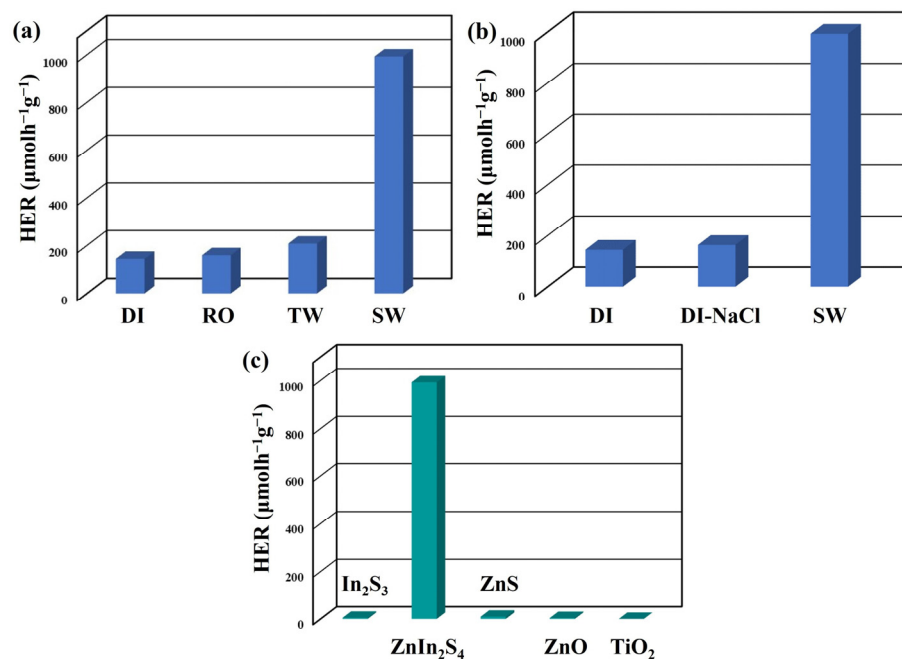
Figure 9. (**a**) The average HER of $ZnIn_2S_4$ nanosheets for the different water sources. (**b**) The average HER of $ZnIn_2S_4$ nanosheets for DI, DI-NaCl, and seawater. (**c**) The average HER of different photocatalysts for seawater.
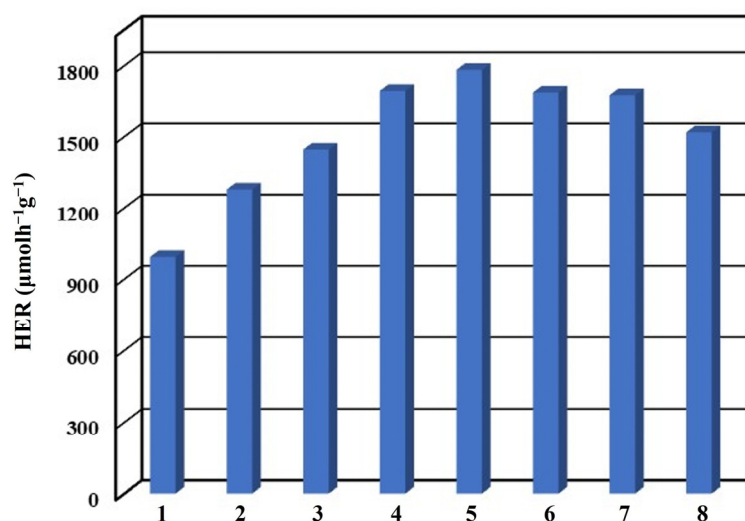
Figure 10. Reusability test of $ZnIn_2S_4$ nanosheets for eight cycles under visible-light irradiation.
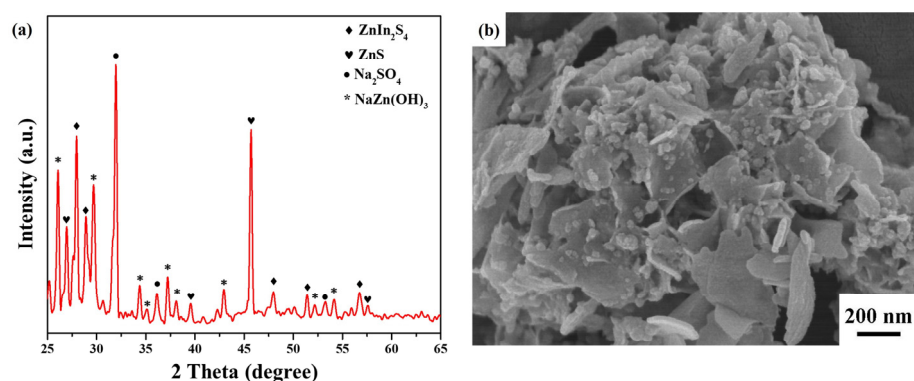
Figure 11. (**a**) XRD pattern and (**b**) FESEM image of $ZnIn_2S_4$ nanosheets after the eighth cycle.

4. Conclusions

This study employed a convenient and rapid microwave-assisted synthesis method to produce In_2S_3 nanosheets, ZnS nanosheets, and $ZnIn_2S_4$ nanosheets with sulfur vacancies. The $ZnIn_2S_4$ nanosheets demonstrated significantly enhanced photocatalytic hydrogen production performance compared to In_2S_3 nanosheets and ZnS nanosheets, achieving approximately 33.3 times and 16.6 times higher activity under visible-light irradiation, respectively. We further investigated the impacts of various factors, such as materials, sacrificial reagents, and pH values, on the photocatalytic hydrogen production of $ZnIn_2S_4$ nanosheets. The $ZnIn_2S_4$ nanosheets exhibited the highest photocatalytic hydrogen production efficiency from seawater, surpassing In_2S_3 nanosheets and ZnS nanosheets by approximately 209.4 times and 106.7 times, respectively. The presence of sulfur vacancies in $ZnIn_2S_4$ nanosheets holds great promise for developing highly efficient and stable photocatalysts for hydrogen production from seawater under visible-light irradiation. This research can potentially conserve precious freshwater resources and use light energy to split seawater into hydrogen energy.

References

1. Gawande, M.B.; Shelke, S.N.; Zboril, R.; Varma, R.S. Microwave-Assisted Chemistry: Synthetic Applications for Rapid Assembly of Nanomaterials and Organics. *Acc. Chem. Res.* **2014**, *47*, 1338–1348. [CrossRef]
2. Wang, J.; Wu, W.; Kondo, H.; Fan, T.; Zhou, H. Recent progress in microwave-assisted preparations of 2D materials and catalysis applications. *Nanotechnology* **2022**, *33*, 342002. [CrossRef]
3. Chang, T.-H.; Chang, Y.-C.; Lee, C.-I.; Lin, Y.-R.; Ko, F.-H. Optimization Temperature Programming of Microwave-Assisted Synthesis ZnO Nanoneedle Arrays for Optical and Surface-Enhanced Raman Scattering Applications. *Nanomaterials* **2022**, *12*, 3989. [CrossRef] [PubMed]
4. Zhu, Y.-J.; Chen, F. Microwave-Assisted Preparation of Inorganic Nanostructures in Liquid Phase. *Chem. Rev.* **2014**, *114*, 6462–6555. [CrossRef] [PubMed]
5. Menon, S.G.; Choudhari, K.S.; Shivashankar, S.A.; Chidangil, S.; Kulkarni, S.D. Microwave solution route to ceramic $ZnAl_2O_4$ nanoparticles in 10 minutes: Inversion and photophysical changes with thermal history. *New J. Chem.* **2017**, *41*, 5420–5428. [CrossRef]

6. Tompsett, G.A.; Conner, W.C.; Yngvesson, K.S. Microwave Synthesis of Nanoporous Materials. *ChemPhysChem* **2006**, *7*, 296–319. [CrossRef]

7. Mirzaei, A.; Neri, G. Microwave-assisted synthesis of metal oxide nanostructures for gas sensing application: A review. *Sens. Actuators B Chem.* **2016**, *237*, 749–775. [CrossRef]

8. Meng, L.-Y.; Wang, B.; Ma, M.-G.; Lin, K.-L. The progress of microwave-assisted hydrothermal method in the synthesis of functional nanomaterials. *Mater. Today Chem.* **2016**, *1–2*, 63–83. [CrossRef]

9. Shen, P.-S.; Tseng, C.-M.; Kuo, T.-C.; Shih, C.-K.; Li, M.-H.; Chen, P. Microwave-assisted synthesis of titanium dioxide nanocrystalline for efficient dye-sensitized and perovskite solar cells. *Sol. Energy* **2015**, *120*, 345–356. [CrossRef]

10. Schwenke, A.M.; Hoeppener, S.; Schubert, U.S. Synthesis and Modification of Carbon Nanomaterials utilizing Microwave Heating. *Adv. Mater.* **2015**, *27*, 4113–4141. [CrossRef] [PubMed]

11. Architha, N.; Ragupathi, M.; Shobana, C.; Selvankumar, T.; Kumar, P.; Lee, Y.S.; Kalai Selvan, R. Microwave-assisted green synthesis of fluorescent carbon quantum dots from Mexican Mint extract for Fe3+ detection and bio-imaging applications. *Environ. Res.* **2021**, *199*, 111263. [CrossRef]

12. Chin, C.D.; Treadwell, L.J.; Wiley, J.B. Microwave Synthetic Routes for Shape-Controlled Catalyst Nanoparticles and Nanocomposites. *Molecules* **2021**, *26*, 3647. [CrossRef]

13. Sharifvaghefi, S.; Zheng, Y. Microwave vs conventional heating in hydrogen production via catalytic dry reforming of methane. *Resour. Chem. Mater.* **2022**, *1*, 290–307. [CrossRef]

14. Motasemi, F.; Ani, F.N. A review on microwave-assisted production of biodiesel. *Renew. Sustain. Energy Rev.* **2012**, *16*, 4719–4733. [CrossRef]

15. Devi, N.; Sahoo, S.; Kumar, R.; Singh, R.K. A review of the microwave-assisted synthesis of carbon nanomaterials, metal oxides/hydroxides and their composites for energy storage applications. *Nanoscale* **2021**, *13*, 11679–11711. [CrossRef] [PubMed]

16. Nayak, S.N.; Bhasin, C.P.; Nayak, M.G. A review on microwave-assisted transesterification processes using various catalytic and non-catalytic systems. *Renew. Energ.* **2019**, *143*, 1366–1387. [CrossRef]

17. Pan, J.; Guan, Z.; Yang, J.; Li, Q. Facile fabrication of $ZnIn_2S_4/SnS_2$ 3D heterostructure for efficient visible-light photocatalytic reduction of Cr(VI). *Chin. J. Catal.* **2020**, *41*, 200–208. [CrossRef]

18. Janani, R.; Preethi, V.R.; Singh, S.; Rani, A.; Chang, C.-T. Hierarchical Ternary Sulfides as Effective Photocatalyst for Hydrogen Generation Through Water Splitting: A Review on the Performance of $ZnIn_2S_4$. *Catalysts* **2021**, *11*, 277. [CrossRef]

19. Yang, R.; Mei, L.; Fan, Y.; Zhang, Q.; Zhu, R.; Amal, R.; Yin, Z.; Zeng, Z. $ZnIn_2S_4$-Based Photocatalysts for Energy and Environmental Applications. *Small Methods* **2021**, *5*, 2100887. [CrossRef]

20. Mamiyev, Z.; Balayeva, N.O. Metal Sulfide Photocatalysts for Hydrogen Generation: A Review of Recent Advances. *Catalysts* **2022**, *12*, 1316. [CrossRef]

21. Wang, J.; Sun, S.; Zhou, R.; Li, Y.; He, Z.; Ding, H.; Chen, D.; Ao, W. A review: Synthesis, modification and photocatalytic applications of ZnIn2S4. *J. Mater. Sci. Technol.* **2021**, *78*, 1–19. [CrossRef]

22. Zhou, H.; Wang, L.; Shi, H.; Zhang, H.; Wang, Y.; Bai, S.; Yang, Y.; Li, Y.; Zhang, T.; Zhang, H. Highly efficient solar-driven photocatalytic hydrogen evolution by a ternary 3D $ZnIn_2S_4$–MoS_2 microsphere/1D TiO_2 nanobelt heterostructure. *New J. Chem.* **2021**, *45*, 14167–14176. [CrossRef]

23. Zhang, G.; Wu, H.; Chen, D.; Li, N.; Xu, Q.; Li, H.; He, J.; Lu, J. A mini-review on $ZnIn_2S_4$-Based photocatalysts for energy and environmental application. *Green Energy Environ.* **2022**, *7*, 176–204. [CrossRef]

24. Chen, Y.; Huang, R.; Chen, D.; Wang, Y.; Liu, W.; Li, X.; Li, Z. Exploring the Different Photocatalytic Performance for Dye Degradations over Hexagonal ZnIn2S4 Microspheres and Cubic $ZnIn_2S_4$ Nanoparticles. *ACS Appl. Mater. Interfaces* **2012**, *4*, 2273–2279. [CrossRef]

25. Chang, Y.-C.; Tasi, C.-L.; Ko, F.-H. Construction of $ZnIn_2S_4/ZnO$ heterostructures with enhanced photocatalytic decomposition and hydrogen evolution under blue LED irradiation. *Int. J. Hydrogen Energy* **2021**, *46*, 10281–10292. [CrossRef]

26. Shen, S.; Zhao, L.; Guan, X.; Guo, L. Improving visible-light photocatalytic activity for hydrogen evolution over $ZnIn_2S_4$: A case study of alkaline-earth metal doping. *J. Phys. Chem. Solids* **2012**, *73*, 79–83. [CrossRef]

27. Shen, J.; Zai, J.; Yuan, Y.; Qian, X. 3D hierarchical $ZnIn_2S_4$: The preparation and photocatalytic properties on water splitting. *Int. J. Hydrogen Energy* **2012**, *37*, 16986–16993. [CrossRef]

28. Sabbah, A.; Shown, I.; Qorbani, M.; Fu, F.-Y.; Lin, T.-Y.; Wu, H.-L.; Chung, P.-W.; Wu, C.-I.; Santiago, S.R.M.; Shen, J.-L.; et al. Boosting photocatalytic CO_2 reduction in a $ZnS/ZnIn_2S_4$ heterostructure through strain-induced direct Z-scheme and a mechanistic study of molecular CO_2 interaction thereon. *Nano Energy* **2022**, *93*, 106809. [CrossRef]

29. Chen, J.; Li, K.; Cai, X.; Zhao, Y.; Gu, X.; Mao, L. Sulfur vacancy-rich $ZnIn_2S_4$ nanosheet arrays for visible-light-driven water splitting. *Mater. Sci. Semicond. Process.* **2022**, *143*, 106547. [CrossRef]

30. Jiao, X.; Chen, Z.; Li, X.; Sun, Y.; Gao, S.; Yan, W.; Wang, C.; Zhang, Q.; Lin, Y.; Luo, Y.; et al. Defect-Mediated Electron–Hole Separation in One-Unit-Cell $ZnIn_2S_4$ Layers for Boosted Solar-Driven CO_2 Reduction. *J. Am. Chem. Soc.* **2017**, *139*, 7586–7594. [CrossRef]

31. Zhang, S.; Liu, X.; Liu, C.; Luo, S.; Wang, L.; Cai, T.; Zeng, Y.; Yuan, J.; Dong, W.; Pei, Y.; et al. MoS_2 Quantum Dot Growth Induced by S Vacancies in a $ZnIn_2S_4$ Monolayer: Atomic-Level Heterostructure for Photocatalytic Hydrogen Production. *ACS Nano* **2018**, *12*, 751–758. [CrossRef] [PubMed]

32. Shen, S.; Chen, J.; Wang, X.; Zhao, L.; Guo, L. Microwave-assisted hydrothermal synthesis of transition-metal doped $ZnIn_2S_4$ and its photocatalytic activity for hydrogen evolution under visible light. *J. Power Sources* **2011**, *196*, 10112–10119. [CrossRef]

33. Zhang, R.; Gong, K.; Cao, S.; Du, F. Amorphous sulfur-rich CoSx nanodots as highly efficient cocatalyst to promote photocatalytic hydrogen evolution over TiO_2. *Int. J. Hydrogen Energy* **2022**, *47*, 39875–39885. [CrossRef]

34. Chen, L.; Wang, D.; Xia, Y.; Liang, R.; Huang, R.; Yan, G. Decoration of nicale phosphide nanoparticles on CdS nanorods for enhanced photocatalytic hydrogen evolution. *Int. J. Hydrogen Energy* **2022**, *47*, 28486–28494. [CrossRef]

35. Chang, Y.-C.; Zeng, C.-J.; Chen, C.-Y.; Tsay, C.-Y.; Lee, G.-J.; Wu, J.J. NiS/Pt loaded on electrospun TiO_2 nanofiber with enhanced visible-light-driven photocatalytic hydrogen production. *Mater. Res. Bull.* **2023**, *157*, 112041. [CrossRef]

36. Liu, Y.; Li, D.; Wan, S.; Wang, F.; Dou, W.; Xu, X.; Li, S.; Ma, R.; Qi, L. A long short-term memory-based model for greenhouse climate prediction. *Int. J. Intell. Syst.* **2022**, *37*, 135–151. [CrossRef]

37. Gruda, N.; Bisbis, M.; Tanny, J. Influence of climate change on protected cultivation: Impacts and sustainable adaptation strategies—A review. *J. Clean. Prod.* **2019**, *225*, 481–495. [CrossRef]

38. Levy, K.; Woster, A.P.; Goldstein, R.S.; Carlton, E.J. Untangling the Impacts of Climate Change on Waterborne Diseases: A Systematic Review of Relationships between Diarrheal Diseases and Temperature, Rainfall, Flooding, and Drought. *Environ. Sci. Technol.* **2016**, *50*, 4905–4922. [CrossRef]

39. Guan, X.; Chowdhury, F.A.; Pant, N.; Guo, L.; Vayssieres, L.; Mi, Z. Efficient Unassisted Overall Photocatalytic Seawater Splitting on GaN-Based Nanowire Arrays. *J. Phys. Chem. C* **2018**, *122*, 13797–13802. [CrossRef]

40. Chen, H.; Li, M.; Gao, J.; Yang, D.; Li, Z.; Liu, H.; Xie, Y.; Guo, L.; Zhou, W. Synergism of sulfur vacancy and Schottky junction in $Ni/ZnIn_2S_4$ nanosheet assembly for efficient charge separation and photocatalytic hydrogen evolution. *Appl. Surf. Sci.* **2023**, *628*, 157385. [CrossRef]

41. Zhang, M.; Tan, P.; Yang, L.; Zhai, H.; Liu, H.; Chen, J.; Ren, R.; Tan, X.; Pan, J. Sulfur vacancy and p-n junction synergistically boosting interfacial charge transfer and separation in $ZnIn_2S_4/NiWO_4$ heterostructure for enhanced photocatalytic hydrogen evolution. *J. Colloid Interface Sci.* **2023**, *634*, 817–826. [CrossRef] [PubMed]

42. Chang, Y.-C.; Chiao, Y.-C.; Fun, Y.-X. $Cu_2O/CuS/ZnS$ Nanocomposite Boosts Blue LED-Light-Driven Photocatalytic Hydrogen Evolution. *Catalysts* **2022**, *12*, 1035. [CrossRef]

43. Corredor, J.; Rivero, M.J.; Rangel, C.M.; Gloaguen, F.; Ortiz, I. Comprehensive review and future perspectives on the photocatalytic hydrogen production. *J. Chem. Technol. Biotechnol.* **2019**, *94*, 3049–3063. [CrossRef]

44. Kumaravel, V.; Imam, M.D.; Badreldin, A.; Chava, R.K.; Do, J.Y.; Kang, M.; Abdel-Wahab, A. Photocatalytic Hydrogen Production: Role of Sacrificial Reagents on the Activity of Oxide, Carbon, and Sulfide Catalysts. *Catalysts* **2019**, *9*, 276. [CrossRef]

45. Lin, Y.-R.; Chang, Y.-C.; Chiao, Y.-C.; Ko, F.-H. Au@CdS Nanocomposites as a Visible-Light Photocatalyst for Hydrogen Generation from Tap Water. *Catalysts* **2022**, *13*, 33. [CrossRef]

46. Markovskaya, D.V.; Cherepanova, S.V.; Saraev, A.A.; Gerasimov, E.Y.; Kozlova, E.A. Photocatalytic hydrogen evolution from aqueous solutions of Na_2S/Na_2SO_3 under visible light irradiation on $CuS/Cd_{0.3}Zn_{0.7}S$ and $NizCd_{0.3}Zn_{0.7}S_1+z$. *Chem. Eng. J.* **2015**, *262*, 146–155. [CrossRef]

47. Bao, N.; Shen, L.; Takata, T.; Domen, K. Self-Templated Synthesis of Nanoporous CdS Nanostructures for Highly Efficient Photocatalytic Hydrogen Production under Visible Light. *Chem. Mater.* **2008**, *20*, 110–117. [CrossRef]

48. Gomathisankar, P.; Hachisuka, K.; Katsumata, H.; Suzuki, T.; Funasaka, K.; Kaneco, S. Photocatalytic hydrogen production with CuS/ZnO from aqueous $Na_2S+Na_2SO_3$ solution. *Int. J. Hydrogen Energy* **2013**, *38*, 8625–8630. [CrossRef]

49. Mills, A.; Le Hunte, S. An overview of semiconductor photocatalysis. *J. Photochem. Photobiol. A Chem.* **1997**, *108*, 1–35. [CrossRef]

50. Safizade, B.; Masoudpanah, S.M.; Hasheminiasari, M.; Ghasemi, A. Photocatalytic activity of $BiFeO_3/ZnFe_2O_4$ nanocomposites under visible light irradiation. *RSC Adv.* **2018**, *8*, 6988–6995. [CrossRef]

51. Chang, Y.-C.; Syu, S.-Y.; Lu, M.-Y. Fabrication of $In(OH)_3–In_2S_3–Cu_2O$ nanofiber for highly efficient photocatalytic hydrogen evolution under blue light LED excitation. *Int. J. Hydrogen Energy* **2023**, *48*, 9318–9332. [CrossRef]

52. Khan, M.S.; Shi, L.; Zou, B.; Ullah, H. Effect of Vanadium doping on optoelectronic and magnetic properties of wurtzite ZnS crystal. *Optik* **2020**, *204*, 164162. [CrossRef]

53. Hezam, A.; Wang, J.; Drmosh, Q.A.; Karthik, P.; Abdullah Bajiri, M.; Namratha, K.; Zare, M.; Lakshmeesha, T.R.; Shivanna, S.; Cheng, C.; et al. Rational construction of plasmonic Z-scheme $Ag-ZnO-CeO_2$ heterostructures for highly enhanced solar photocatalytic H_2 evolution. *Appl. Surf. Sci.* **2021**, *541*, 148457. [CrossRef]

54. Munawar, K.; Mansoor, M.A.; Olmstead, M.M.; Zaharinie, T.; Mohd Zubir, M.N.; Haniffa, M.; Basirun, W.J.; Mazhar, M. Fabrication of Ag-ZnO composite thin films for plasmonic enhanced water splitting. *Mater. Chem. Phys.* **2020**, *255*, 123220. [CrossRef]

55. Trang, T.N.Q.; Phan, T.B.; Nam, N.D.; Thu, V.T.H. In Situ Charge Transfer at the Ag@ZnO Photoelectrochemical Interface toward the High Photocatalytic Performance of H_2 Evolution and RhB Degradation. *ACS Appl. Mater. Interfaces* **2020**, *12*, 12195–12206. [CrossRef] [PubMed]

56. Motora, K.G.; Wu, C.-M.; Chala, T.F.; Chou, M.-H.; Kuo, C.-F.J.; Koinkar, P. Highly efficient photocatalytic activity of $Ag_3VO_4/WO_{2.72}$ nanocomposites for the degradation of organic dyes from the ultraviolet to near-infrared regions. *Appl. Surf. Sci.* **2020**, *512*, 145618. [CrossRef]

57. Zhang, D.; Liang, S.; Yao, S.; Li, H.; Liu, J.; Geng, Y.; Pu, X. Highly efficient visible/NIR photocatalytic activity and mechanism of Yb3+/Er3+ co-doped $Bi_4O_5I_2$ up-conversion photocatalyst. *Sep. Purif. Technol.* **2020**, *248*, 117040. [CrossRef]

58. Cui, L.; Ding, X.; Wang, Y.; Shi, H.; Huang, L.; Zuo, Y.; Kang, S. Facile preparation of Z-scheme WO_3/g-C_3N_4 composite photocatalyst with enhanced photocatalytic performance under visible light. *Appl. Surf. Sci.* **2017**, *391*, 202–210. [CrossRef]

59. Li, Y.; Wang, R.; Li, H.; Wei, X.; Feng, J.; Liu, K.; Dang, Y.; Zhou, A. Efficient and Stable Photoelectrochemical Seawater Splitting with TiO_2@g-C_3N_4 Nanorod Arrays Decorated by Co-Pi. *J. Phys. Chem. C* **2015**, *119*, 20283–20292. [CrossRef]

60. Peng, H.; Liu, D.; Zheng, X.; Fu, X. N-Doped Carbon-Coated ZnS with Sulfur-Vacancy Defect for Enhanced Photocatalytic Activity in the Visible Light Region. *Nanomaterials* **2019**, *9*, 1657. [CrossRef]

61. Zhou, J.; Zhao, J.; Liu, R. Defect engineering of zeolite imidazole framework derived ZnS nanosheets towards enhanced visible light driven photocatalytic hydrogen production. *Appl. Catal. B Environ.* **2020**, *278*, 119265. [CrossRef]